

Quantum ghost imaging using asynchronous detection: supplement

**CARSTEN PITSCH,^{1,2,*} DOMINIK WALTER,¹ SIMON GROSSE,³
WERNER BROCKHERDE,³ HELGE BÜRSING,¹ AND MARC
EICHHORN^{1,2}**

¹*Fraunhofer Institute of Optonics, System Technologies and Image Exploitation (IOSB), Gutleuthausstr. 1, 76275 Ettlingen, Germany*

²*Institute of Control Systems (IRS), Karlsruhe Institute of Technology, Fritz-Haber-Weg 1, 76131 Karlsruhe, Germany*

³*Fraunhofer Institute for Microelectronic Circuits and Systems (IMS), Finkenstr. 61, 47057 Duisburg, Germany*

*Corresponding author: carsten.pitsch@iosb.fraunhofer.de

This supplement published with The Optical Society on 11 June 2021 by The Authors under the terms of the [Creative Commons Attribution 4.0 License](#) in the format provided by the authors and unedited. Further distribution of this work must maintain attribution to the author(s) and the published article's title, journal citation, and DOI.

Supplement DOI: <https://doi.org/10.6084/m9.figshare.14665131>

Parent Article DOI: <https://doi.org/10.1364/AO.423634>

Quantum ghost imaging using asynchronous detection:

supplemental document

In this supplementary file we show more details to some of our methods for improvement of the system described in our paper, namely the post-processing scheme used to correct the timing information of the SPAD and the steps and methods used for background reduction.

1. TIMING CORRECTION

The timing information of the described SPAD detector is referenced to the beginning of the measurement and consists of 3 parameters, an 8-bit COARSE value, which returns the detection time with a resolution of 5ns and two 4-bit fine values. These fine values are called START and STOP and return the time to the COARSE value or the end of measurement respectively with a resolution of 312.5 ps.

The final timestamp is then given by the following equation:

$$T = [16 * COARSE + START - STOP] * 312.5ps \quad (S1)$$

Adding this value to the global timestamp of the dedicated measurement window, registered by appropriate time-correlated single-photon-counting (TCSPC) electronics, returns the global timestamp of the detected photon. This value will then be compared to the timestamps of the detected IR-photons, obtained by registering their signal using the same TCSPC electronics. Detecting both photons of the entangled photon pairs will lead to a peak of coincidences over time due to the fixed path length difference of the entangled photons.

As mentioned, during analysis of these coincidence measurements, a dependence of the position of this coincidence peak on the timing parameters of the SPAD array was found. Using a sufficiently long coincidence measurement, whose uncorrected coincidence peak is shown in figure S1, we filtered the data based on specific START and STOP values. By doing so, we could identify the quite broad, uncorrected coincidence peak of figure S1 as multitude of individual fine peaks, each with specific temporal offsets. Further analysis showed these offsets to be linked to the specific combination of the START and STOP values, a selection of which is shown in figure S2.

We verified this behaviour and its predictability with multiple coincidence measurements, all of which showed specific offsets for specific START-STOP combinations.

Using this analysis, we could obtain a dedicated "Correction-Matrix", which corrects the delay for every further measurement and improved our timing and therefore our depth resolution by roughly a factor of 3.

At first glance this problem does not seem very obvious, however, in previous measurements, we used a prototype of this detector, in which the problem was more prevalent. This prototype also had a drift of the coincidence peak over the coarse values, as shown in figure S3, due to which we were first able to identify the problem and program our Correction-Matrix. This is also the reason we chose a 2D representation over the COARSE value for the data shown here.

2. BACKGROUND REDUCTION

As stated in the text we can use the temporal evaluation of photons shown in figure 4 of the paper to extract the distribution of background photons and derive some of the effects degrading the image quality in order to suppress their effects.

To do so we isolate all the photons contained in Δt_{nc1} and Δt_{nc2} and extract their spatial distribution f_{BG} , given by the pixel position. This results in the image shown in figure S5(a) and corresponds to the image one would obtain without the information of the idler photon.

This distribution is a superposition of the actual SPDC emission as well as detector noise and the pixel dependent detection efficiencies as shown in equation 2 of the paper.

In order to estimate the detector noise distribution σ_{px} it has shown to be most simple to perform a short reference measurement with a switched off laser, the result of which is shown in figure S5, and weight the absolute values of the results according to the size of the time windows.

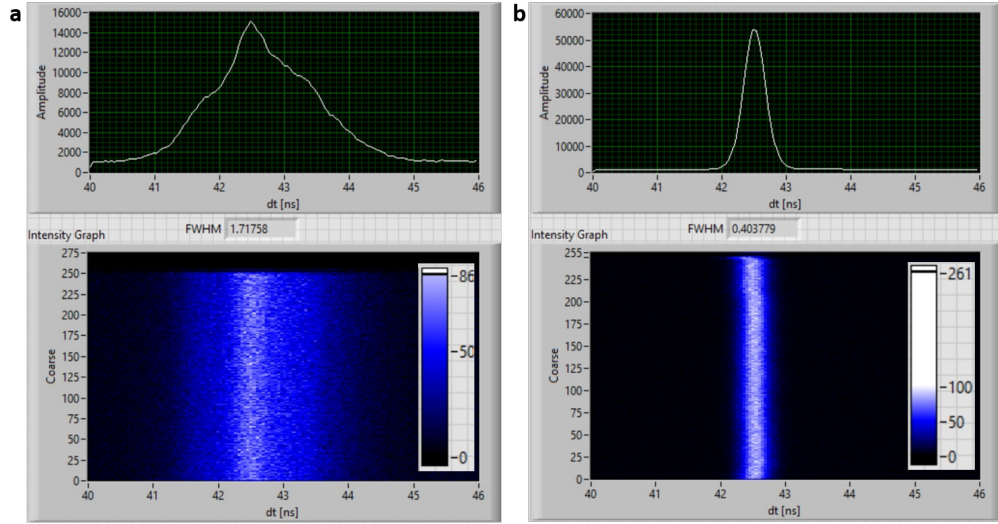


Fig. S1. Detailed view of the temporal coincidence detection. In the upper images one can see the coincidence peak integrated over all COARSE values and in the lower images one can see the temporal progression of the coincidence peak in dependence of the COARSE value for the detector used in this work. (a) Uncorrected, raw coincidence detection with a FWHM of 1.7 ns and a full peak width of roughly 3.5 ns. (b) Corrected, raw coincidence detection with a FWHM of 0.4 ns and a full peak width of roughly 1 ns

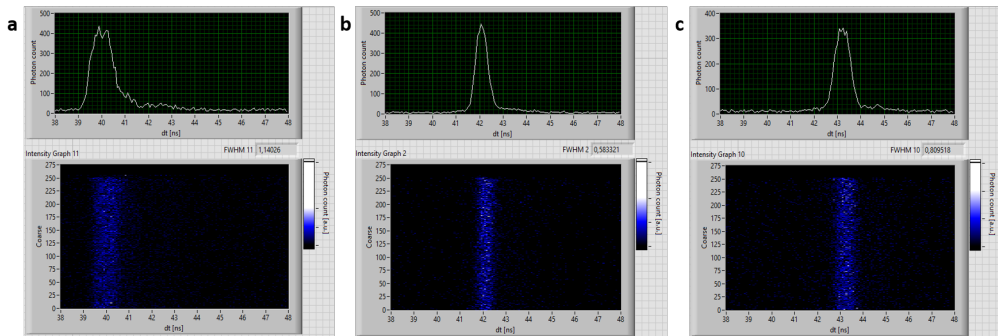


Fig. S2. Selection of the results obtained by filtering the coincidence evaluation of S1 according to the START and STOP parameters. One can clearly see, that the coincidence peak is shifted and its FWHM is dependent on these parameters. The shift and broadening are constant over all the coarse values (a) coincidence evaluation for START = 12 and STOP = 10. (b) coincidence evaluation for START = 1 and STOP = 0. (c) coincidence evaluation for START = 0 and STOP = 8.

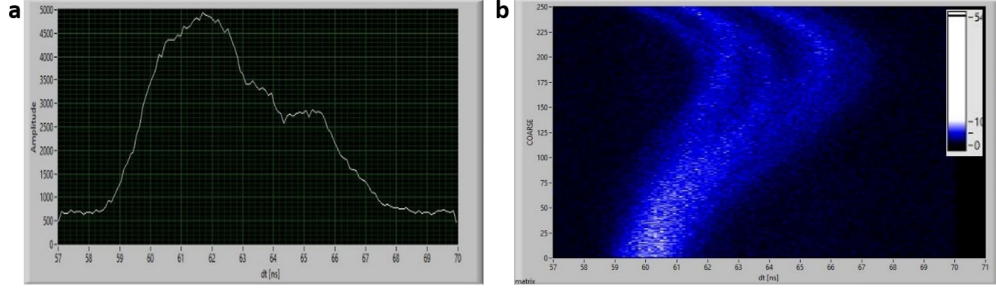


Fig. S3. Coincidence evaluation with the first prototype of the detector. (a) Coincidence evaluation integrated over all COARSE values of the detector (b) Temporal progression of the coincidence peak in dependence of the COARSE values. One can clearly see a drift of the coincidence as well as a broadening of the peak towards higher COARSE values. Looking closer one can also distinguish multiple lines, each with a specific coincidence drift and offset. In the new detector version the drift does not occur, however there is still some coincidence offset, as seen in figure S2.

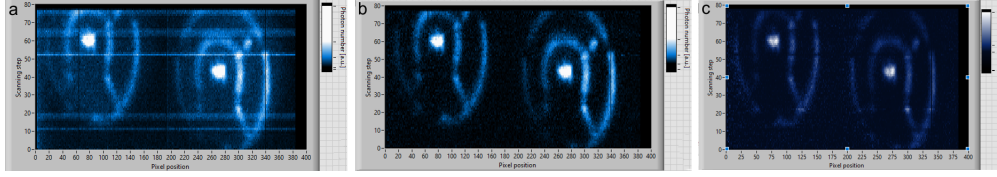


Fig. S4. Coincidence image captured at various stages of post-processing. (a) raw image resulting from evaluating Δt_c as shown in figure 4 of the paper, the brighter horizontal lines are explained in S5. (b) image after subtraction of the background data obtained by evaluating Δt_{nc} and shown in S5(a). (c) Image after weighting the result of (b) according to equation 3 of the paper using the SPDC emission shown in figure S5(c) and an appropriate Gaussian weight for estimation of the IR incoupling.

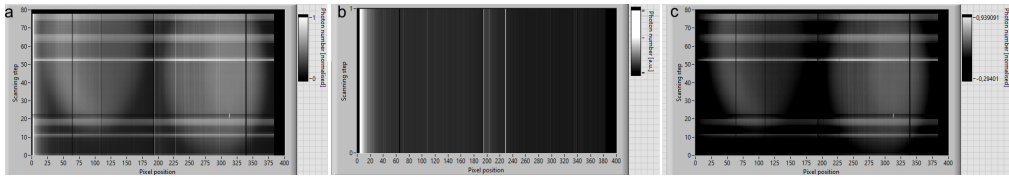


Fig. S5. Data used for estimation of background, noise and SPDC emission. The most noisy pixels (Threshold: noise 50 times average noise) have been filtered out during image acquisition and can be seen as black vertical lines in all images. The bright horizontal lines are measurements during which our shared laboratory was in use, leading to increased stray light and thus increasing the noise of the SPAD. (a) raw image of the background noise resulting from evaluating Δt_{nc} as shown in figure 4 of the paper. This corresponds to the image a regular camera would obtain without the idler information. (b) dark noise distribution of the SPAD array, obtained by completely darkening the setup and just running the detection. Due to technical reasons individual detectors have highly varying noise distributions, thus this estimation is only valid for the specific detector used. The "slope" toward the beginning of the line is a hardware effect, which has only been observed in the detector chip used here. (c) Estimated SPDC detection obtained by subtracting (b) from (a). This estimation does not only contain the actual SPDC emission, but is also weighted by the pixel dependent detection efficiency. It has been used to weight the image S4(c) according to equation 3 of the paper.

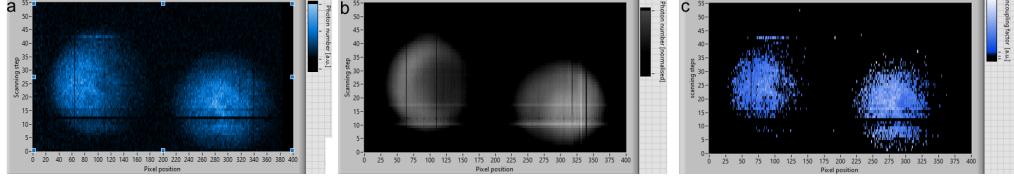


Fig. S6. Result of the reference measurement in order to determine the incoupling of the fiber-bound IR-detector. (a) raw image resulting from evaluating Δt_c . Since no target was present, the result should ideally directly correspond to the SPDC emission. (b) estimation of the SPDC detection obtained by evaluating Δt_{nc} and subtracting the dark noise as in S5 (c) Estimation of the coupling of SPDC emission and the fiber of the IR detector. It was obtained by weighting the coincidence image of (a) with the SPDC estimation of (b). A gaussian was subsequently fitted to this data and used to weight the final image shown in S4(c).

The resulting distribution yields the actual SPDC emission weighted by the pixel dependent detection efficiency, as described in equation 3 of the paper and shown in figure S5(c).

As discussed in the paper, one should, for a complete estimation of the image degradation effects, also take in account the detection and collection efficiency of the IR SPAD. In order to do this, we made a dedicated reference measurement by scanning the SPDC emission without a target present in the idler arm. From the resulting coincidence image at the SPAD, we were able to estimate the efficiencies by comparing both the SPDC emission at the SPAD and the resulting coincidence image and weighting them accordingly as shown in figure S6. This lead us to a gaussian approximation of the incoupling, which was expected since the IR-SPAD consists of a fiber-coupled detector.